A. Susperregui, M. I. Martínez, G. Tapia-Otaegui and A. Etxeberria, "Sliding-Mode Control Algorithm for DFIG Synchronization to Unbalanced and Harmonically Distorted Grids," in **IEEE Transactions on Sustainable Energy**, vol. 13, no. 3, pp. 1566-1579, July 2022, doi: 10.1109/TSTE.2022.3166217

Sliding-Mode Control Algorithm for DFIG Synchronization to Unbalanced and Harmonically Distorted Grids

Ana Susperregui, *Member, IEEE,* M. Itsaso Martínez, Gerardo Tapia-Otaegui, and Aitor Etxeberria

***Abstract*—In order to smoothly connect to permanently disturbed grids, DFIG-based wind turbines must precisely synchronize the voltage induced at their open stator with that of the grid. Hence, aiming at addressing the still unpublished task of synchronizing DFIGs to simultaneously unbalanced and harmonically distorted grids, a phase-locked loop (PLL)-less and naturally chatter-free sliding-mode control (SMC) algorithm is proposed. The strategies developed so far were formulated considering synchronous reference frames. However, by designing a stationary reference frame-based solution, decomposition into positive- and negative-sequences and harmonic components is avoided. As a result, a relatively straightforward control structure with strong potential for industrialization is obtained, consisting of a single voltage loop per component with just one parameter to be tuned. The stability and robustness resulting from its application are analytically studied under both uncertainties and disturbances. Additionally, a simple method for rotor positioning, independent of grid disturbances, is provided. Simulation over a 2-MW DFIG model and rapid control prototyping (RCP) over a 7-kW DFIG experimental rig are carried out. In this way, the performance and robustness of the suggested control scheme are validated under both unbalanced and harmonically distorted grid voltage, substantial parameter deviations, and varying wind speed and grid frequency profiles.**

***Index Terms*—Doubly-fed induction generator (DFIG), harmonic distortion, rotor positioning, robustness, sliding-mode control (SMC), synchronization, unbalanced grid voltage.**

NOMENCLATURE

C	DC link capacitance.
f	Grid frequency.
i_r, i_s	Components of rotor and stator current space-vectors.
$\boldsymbol{i}_r$, $\boldsymbol{i}_s$	Rotor and stator current space-vectors.
L_g	Grid filter inductance.
L_{lr}, L_{ls}	Rotor and stator leakage inductances.
L_m, L_r, L_s	Magnetizing, rotor and stator inductances.
n	Stator to rotor turn-ratio.
P	Number of pole pairs.
R_g, R_r, R_s	Grid filter, rotor and stator resistances.
t	Time.
t_{reach}	Time required to reach the sliding regime.
v_g, v_r, v_s	Components of grid, rotor and stator voltage space-vectors.
$\boldsymbol{v}_r$, $\boldsymbol{v}_s$	Rotor and stator voltage space-vectors.
V_{dc}	DC link voltage.
$V_{g\,rms}$	Rated root mean square value of the grid phase voltage.
Δ	Deviation from expected value.
θ_r, θ_{rm}	Rotor electrical and mechanical angular positions.
θ_{re}, θ_{rme}	Rotor electrical and mechanical angular positions derived from the encoder.
$\boldsymbol{\psi}_r$, $\boldsymbol{\psi}_s$	Rotor and stator flux space-vectors.
ω_r, ω_{rm}	Rotor electrical and mechanical angular speeds.

Subscripts

d, q	Direct- and quadrature-axis components, expressed in the stationary reference frame.
eq	Equivalent control term.
SMC	Control term containing the sign function.
α, β	Direct- and quadrature-axis components, expressed in the rotor natural reference frame.
0	Nominal value.

Superscripts

$*$	Reference value.
$\wedge$	Expected or estimated value.

This work was co-financed by the Spanish Ministry of Science and Innovation —project code PID2020-115484RA-I00—, FEDER Funds, EU, and by the Basque Government under research grant IT1256-19.

A. S., M. I. M. and G. T.-O. are with the Department of Automatic Control and Systems Engineering (DACSE), University of the Basque Country UPV/EHU, Faculty of Engineering–Gipuzkoa (FEG), Donostia 20018, Spain (e-mail: ana.susperregui@ehu.eus; mirenitsaso.martinez@ehu.eus; gerardo.tapia@ehu.eus).

A. E. was with the DACSE, UPV/EHU, FEG, Donostia 20018, Spain. He is now with Orona EIC, Hernani 20120, Spain (e-mail: aetxeberriau@orona-group.com).

I. INTRODUCTION

NOWADAYS, wind, together with hydro and solar photovoltaic, are the most widely used renewable energy sources for power generation worldwide [1]. Focusing on wind, there are two main sectors: the still prevailing onshore and the strongly rising offshore wind farms. Several components conform a wind energy conversion system (WECS), *inter alia*, the electrical generator + power converter set, available in a variety of topologies [2].

In the middle of the last decade, despite the high penetration of the permanent-magnet synchronous generator (PMSG) + full converter topology, especially in offshore, the DFIG configuration was still prevalent [3]. Even today, according to the statistics on the wind turbine types installed by the world's leading manufacturer, those containing a DFIG are still very

significant [4]. Thus, further research on this configuration aimed at improving its performance seems justified [5], [6].

Prior to grid-connected operation, the stator voltage of the DFIG must be synchronized to that of the grid in magnitude, frequency and phase to achieve a smooth connection, hence preventing high inrush currents in the stator [7]. However, a thorough literature review encompassing the last two decades reveals that this problem has received little attention from the research community, as corroborated in [8]–[10], especially when compared to the grid-connected operation of the DFIG, which has given rise to countless publications.

Among the most relevant works identified on DFIG grid synchronization, some of the pioneers propose proportional-integral (PI) regulator-based conventional control structures for the rotor-side converter (RSC). For instance, in [11]–[14], synchronization is achieved by controlling the rotor current, and a cascaded outer voltage loop is incorporated in [15]. Considering also the robustness against parameter variation, [16] performs a modification of the typical PI-based power control scheme by adding some compensation terms to the inner current loops. Along the same lines, seeking that the set-point of the direct rotor current component does not depend on the magnetizing inductance, [17] outlines a control scheme intended to derive such set-point by cascading an outer control-loop that regulates the quadrature component of the induced stator voltage.

Direct torque control (DTC) has been adopted in [18], where the references for the switching table are calculated by means of PI-based control loops. In contrast, [19] applies a PI-independent direct virtual torque control (DVTC) strategy, derived from DTC, where no stator voltage measurement is required. Moreover, other solutions have also been proposed based on direct voltage control (DVC) [8], [20], [21] or even on model predictive control (MPC) [10], [22]. In particular, besides presenting a synchronization method, the effect of varying the DFIG's mutual inductance during such operating regime is analyzed in [10].

Similar to this paper, aiming at conferring high robustness in the face of disturbances and uncertainties, both parametric and unstructured, the sliding-mode control (SMC) approach has also been adopted. Several different SMC strategies are found in the literature, such as the integral SMC (ISMC) presented in [23] and [24], or the higher-order SMC (HOSMC) algorithm referred to as super-twisting for current [25] or voltage control [9]. Regarding those solutions based exclusively on current regulation, such as that proposed in [25], their main weakness lies in the fact that precise knowledge of the magnetizing inductance is needed to properly fix the rotor current set-point leading to correct synchronization. In the case of [25], this requirement greatly spoils the degree of robustness achieved with the adoption of SMC.

In this context, the SMC-based synchronization schemes put forward in [23], [24] and [9] opt for directly controlling the stator voltage, hence avoiding the use of current loops. Apart from the order and format of the SMC laws implemented, probably the most significant difference between these solutions consists in the way the rotor and stator voltage components are paired. In [24] and [9], the direct and quadrature components of the stator voltage are respectively governed by the direct and quadrature rotor voltage components. In contrast, based on the relative gain array (RGA) methodology, [23] proposes to control the direct component of the stator voltage by means of the quadrature rotor voltage component, and *vice versa*. Although both approaches lead to satisfactory simulation results when facing three-phase balanced sinusoidal grid voltages, such results are confirmed experimentally only in [23].

It must also be considered that certain margins of imbalance and harmonic distortion of the grid voltage are allowed in continuous operation of distributed energy resources (DER) [7], [26]–[28]. Therefore, the DFIG should be able to achieve synchronization even under the aforementioned permanent but bounded disturbances, in order to smoothly connect to the grid.

However, based on the broad experience gained by the research community from the grid-connected operation of the DFIG [29], [30], it can be concluded that none of the solutions cited so far could effectively synchronize the DFIG to grids whose voltage is either unbalanced [31]–[33] or harmonically distorted. Indeed, having been designed in the synchronous reference frame considering only the positive sequence, they are not conceived to face such operating conditions. Furthermore, few have tackled the rotor positioning task, as well as the effects of both parametric deviations or operation under common disturbances, such as varying wind speed and grid frequency profiles.

With the aim of facing grid voltage imbalances, a design based solely on PI current regulators is presented in [33], thus requiring precise knowledge of the magnetizing inductance. In pursuit of the same objective, [32] suggests implementing a cascade control strategy where the inner loops rely on multivariable state feedback (MSF) current controllers, while the outer loops regulate the induced stator voltage via PIs. Similarly, an improved and successful variant of [23] is introduced in [31] by incorporating pure integral (I) controllers to regulate the negative sequence. Nonetheless, in addition to the decomposition of rotor current and grid voltage —and also of stator voltage, in the case of [31], [32]— into positive- and negative-sequences, the separate control of both sequences is required in the three aforementioned solutions. As a result, not only the complexity of the RSC control scheme itself increases, but also the number of parameters to be tuned —a minimum of seven in the most favorable case. Despite all this, neither of them would be able to efficiently cope with grids whose voltage is simultaneously unbalanced and harmonically distorted, as pure I or even PI controllers running in synchronous frames are known to be ineffective in presence of harmonic distortion [34].

In an attempt to address the challenge of DFIG synchronization under permanently disturbed grids, this paper proposes a SMC-based strategy whose main contributions are as follows:

- Ability to track simultaneously unbalanced and harmonically distorted grid voltages so as to induce a replica of such voltages at the open stator terminals.
- The high responsiveness conferred by SMC enables a design according to the stationary reference frame, in which no extraction of positive- and negative-sequences

or harmonic components is required, phase-locked loop (PLL) algorithms are avoided, and almost no Park's transforms are needed —only one involving just the rotor electrical position.
- The above-mentioned features make the implementation of the control algorithm straightforward and, therefore, highly industrializable, as it is naturally chatter-free and relies on a single voltage control-loop with just one parameter to be tuned.
- Robustness under substantial parameter deviations and usual disturbances, such as wind speed variations and fluctuations in the grid frequency.
- A simple method for rotor positioning is provided, which is independent of any disturbance present in the grid.

In order to present the proposed control scheme and its performance, the rest of the paper has been structured as follows. Section II provides the mathematical model of the DFIG and then proceeds to the design of the SMC scheme, whose stability and robustness are also analyzed. In addition, a simple solution for rotor positioning is described. Simulation and experimental results validating the suggested algorithm are respectively provided in Sections III and IV. Finally, conclusions are drawn in Section V.

II. Modeling and control design

A. DFIG model for grid synchronization

According to both the stationary reference frame and the nomenclature adopted by [35], the stator and rotor voltage equations of the DFIG can be represented by [36]

$$\boldsymbol{v}_{sdq} = R_s \boldsymbol{i}_{sdq} + \dot{\boldsymbol{\psi}}_{sdq} \tag{1}$$

$$\boldsymbol{v}_{rdq} = R_r \boldsymbol{i}_{rdq} + \dot{\boldsymbol{\psi}}_{rdq} - j\omega_r \boldsymbol{\psi}_{rdq}, \tag{2}$$

where the stator and rotor fluxes are, respectively,

$$\boldsymbol{\psi}_{sdq} = L_s \boldsymbol{i}_{sdq} + L_m \boldsymbol{i}_{rdq} \tag{3}$$

$$\boldsymbol{\psi}_{rdq} = L_r \boldsymbol{i}_{rdq} + L_m \boldsymbol{i}_{sdq}. \tag{4}$$

Considering, on the one hand, that the stator current is non-existent —$\boldsymbol{i}_{sdq} = \boldsymbol{0}$— when the DFIG is disconnected from the grid, and, on the other, the expressions for stator and rotor fluxes (3) and (4), the model in (1) and (2) may be rewritten as follows:

$$\boldsymbol{v}_{sdq} = L_m \dot{\boldsymbol{i}}_{rdq} \tag{5}$$

$$\boldsymbol{v}_{rdq} = R_r \boldsymbol{i}_{rdq} + L_r \dot{\boldsymbol{i}}_{rdq} - j\omega_r L_r \boldsymbol{i}_{rdq}, \tag{6}$$

where (5) evidences that, in order to induce an adequate voltage level in the stator, the rotor current should not undergo abrupt changes.

Given that it is intended to directly control —with no inner current loops— the voltage induced at the open stator terminals through the voltage applied to the rotor windings, the model given by (5) and (6) can be rearranged as

$$\boldsymbol{v}_{sdq} = \frac{L_m}{L_r}\left(-R_r \boldsymbol{i}_{rdq} + j\omega_r L_r \boldsymbol{i}_{rdq} + \boldsymbol{v}_{rdq}\right) \tag{7}$$

after solving the time derivative of the rotor current space-vector, $\dot{\boldsymbol{i}}_{rdq}$, from (6) and subsequently replacing it in (5). Finally, splitting (7) into the d-q components leads to

$$v_{sd} = \frac{L_m}{L_r}\left(-R_r i_{rd} - \omega_r L_r i_{rq} + v_{rd}\right) \tag{8}$$

$$v_{sq} = \frac{L_m}{L_r}\left(-R_r i_{rq} + \omega_r L_r i_{rd} + v_{rq}\right). \tag{9}$$

B. Proposed SMC control strategy

Aiming at integrating the aspect of robustness in the design process, the model in (8) and (9) is completed as follows:

$$v_{sd} = \frac{L_m}{L_r}\left(-R_r i_{rd} - \omega_r L_r i_{rq} + v_{rd}\right) + \mu_d \tag{10}$$

$$v_{sq} = \frac{L_m}{L_r}\left(-R_r i_{rq} + \omega_r L_r i_{rd} + v_{rq}\right) + \mu_q, \tag{11}$$

where functions $\mu_d\left(i_{rd},\ i_{rq},\ \omega_r,\ t\right)$ and $\mu_q\left(i_{rd},\ i_{rq},\ \omega_r,\ t\right)$ represent the effect of lumped disturbances and unmodeled dynamics. To account also for parametric uncertainty, it will be assumed that R_r, L_m and L_r correspond to the actual values of those parameters, while $\hat{R}_r$, $\hat{L}_m$ and $\hat{L}_r$ are their respective values in the designer's mind. Accordingly,

$$R_r = \hat{R}_r + \Delta R_r;\ \ L_m = \hat{L}_m + \Delta L_m;\ \ L_r = \hat{L}_r + \Delta L_r, \tag{12}$$

with ΔR_r, ΔL_m and ΔL_r representing the parameter deviations with respect to $\hat{R}_r$, $\hat{L}_m$ and $\hat{L}_r$, respectively.

In order to synchronize the DFIG to the grid even in presence of both imbalances and harmonic distortion —permanently disturbed grid voltage—, the following switching functions are selected:

$$s_d = v_{sd}^* - v_{sd} \tag{13}$$

$$s_q = v_{sq}^* - v_{sq}. \tag{14}$$

Taking the time derivatives of (13) and (14), and considering (10) and (11), the system dynamics are transferred to the switching variables as follows:

$$\dot{s}_d = \dot{v}_{sd}^* + \frac{L_m}{L_r}\left[R_r \dot{i}_{rd} + L_r\left(\dot{\omega}_r i_{rq} + \omega_r \dot{i}_{rq}\right) - \dot{v}_{rd}\right] + m_d \tag{15}$$

$$\dot{s}_q = \dot{v}_{sq}^* + \frac{L_m}{L_r}\left[R_r \dot{i}_{rq} - L_r\left(\dot{\omega}_r i_{rd} + \omega_r \dot{i}_{rd}\right) - \dot{v}_{rq}\right] + m_q, \tag{16}$$

with $m_d = -\dot{\mu}_d$ and $m_q = -\dot{\mu}_q$, evincing that the system has zero relative order [37], since the time derivatives of the control signals, $\dot{v}_{rd}$ and $\dot{v}_{rq}$, appear explicitly in (15) and (16). Nevertheless, the change of variables given next:

$$u_d = \dot{v}_{rd} \rightarrow v_{rd} = \int_0^t u_d(\tau)d\tau \tag{17}$$

$$u_q = \dot{v}_{rq} \rightarrow v_{rq} = \int_0^t u_q(\tau)d\tau, \tag{18}$$

together with the consideration of u_d and u_q as the new control signals, lead the system to become of relative order one.

In this context, standard or first-order sliding-mode control (1-SMC) could be applied to solve the control problem. However, with the intention of reducing the control effort of a pure 1-SMC algorithm, an equivalent control term [38] is also incorporated, which represents the value of the control

signal required to preserve the sliding regime, $s_d = s_q = 0$, in absence of disturbances and uncertainties. That is,

$$u_d = u_{d_{eq}} + u_{d_{SMC}} \tag{19}$$

$$u_q = u_{q_{eq}} + u_{q_{SMC}}. \tag{20}$$

Therefore, by virtue of (17) and (18), the voltage to be applied to the rotor windings can be obtained by time integration of (19) and (20), thus giving rise to

$$v_{rd} = \overbrace{\int_0^t u_{d_{eq}}(\tau)d\tau}^{v_{rd_{eq}}} + \overbrace{\int_0^t u_{d_{SMC}}(\tau)d\tau}^{v_{rd_{SMC}}} \tag{21}$$

$$v_{rq} = \underbrace{\int_0^t u_{q_{eq}}(\tau)d\tau}_{v_{rq_{eq}}} + \underbrace{\int_0^t u_{q_{SMC}}(\tau)d\tau}_{v_{rq_{SMC}}}. \tag{22}$$

The equivalent control terms given next can be derived by the designer after forcing both (15) and (16) to zero and subsequently solving for $\dot{v}_{rd} = u_d$ and $\dot{v}_{rq} = u_q$:

$$u_{d_{eq}} = \dot{v}_{rd_{eq}} = \frac{\hat{L}_r}{\hat{L}_m}\dot{v}^*_{sd} + \hat{R}_r\dot{i}_{rd} + \hat{L}_r\left(\dot{\omega}_r i_{rq} + \omega_r\dot{i}_{rq}\right) \tag{23}$$

$$u_{q_{eq}} = \dot{v}_{rq_{eq}} = \frac{\hat{L}_r}{\hat{L}_m}\dot{v}^*_{sq} + \hat{R}_r\dot{i}_{rq} - \hat{L}_r\left(\dot{\omega}_r i_{rd} + \omega_r\dot{i}_{rd}\right), \tag{24}$$

where uncertainties and disturbances have been disregarded —$m_d = m_q = 0$; $R_r = \hat{R}_r$; $L_m = \hat{L}_m$; $L_r = \hat{L}_r$— in coherence with the definition of equivalent control. Subsequent time integration of (23) and (24) leads to

$$v_{rd_{eq}} = \frac{\hat{L}_r}{\hat{L}_m}v^*_{sd} + \hat{R}_r i_{rd} + \omega_r\hat{L}_r i_{rq} \tag{25}$$

$$v_{rq_{eq}} = \frac{\hat{L}_r}{\hat{L}_m}v^*_{sq} + \hat{R}_r i_{rq} - \omega_r\hat{L}_r i_{rd}. \tag{26}$$

Moreover, the relation between rotor current and stator voltage shown in (5) allows rewriting (25) and (26) as expressions relying solely on voltage; i.e.,

$$v_{rd_{eq}} = \frac{\hat{L}_r}{\hat{L}_m}v^*_{sd} + \frac{\hat{R}_r}{\hat{L}_m}\int_0^t v_{sd}(\tau)d\tau + \omega_r\frac{\hat{L}_r}{\hat{L}_m}\int_0^t v_{sq}(\tau)d\tau \tag{27}$$

$$v_{rq_{eq}} = \frac{\hat{L}_r}{\hat{L}_m}v^*_{sq} + \frac{\hat{R}_r}{\hat{L}_m}\int_0^t v_{sq}(\tau)d\tau - \omega_r\frac{\hat{L}_r}{\hat{L}_m}\int_0^t v_{sd}(\tau)d\tau. \tag{28}$$

Note that, as a result of the trivial switching functions selected in (13) and (14), the voltage errors are equal to zero in the sliding regime, meaning that $v_{sd} = v^*_{sd}$ and $v_{sq} = v^*_{sq}$. Hence, bearing in mind that the equivalent control aims precisely at contributing to the preservation of the sliding regime, (27) and (28) may be approximated as

$$v_{rd_{eq}} \simeq \frac{\hat{L}_r}{\hat{L}_m}v^*_{sd} + \frac{\hat{R}_r}{\hat{L}_m}\int_0^t v^*_{sd}(\tau)d\tau + \omega_r\frac{\hat{L}_r}{\hat{L}_m}\int_0^t v^*_{sq}(\tau)d\tau \tag{29}$$

$$v_{rq_{eq}} \simeq \frac{\hat{L}_r}{\hat{L}_m}v^*_{sq} + \frac{\hat{R}_r}{\hat{L}_m}\int_0^t v^*_{sq}(\tau)d\tau - \omega_r\frac{\hat{L}_r}{\hat{L}_m}\int_0^t v^*_{sd}(\tau)d\tau, \tag{30}$$

thus taking the form of typical feedforward-like control terms that depend only on the references of the stator voltage components.

It must be highlighted that, regardless of the pair of expressions adopted to compute the equivalent control terms —(25)-(26), (27)-(28) or (29)-(30)—, their calculation is adversely affected by any discrepancy between $\hat{R}_r$, $\hat{L}_m$ and $\hat{L}_r$ and their respective actual values, R_r, L_m and L_r. Obviously, the larger those mismatches are, the less accurate the computed $v_{rd_{eq}}$ and $v_{rq_{eq}}$ terms will be, hence increasing the control effort to be made by the $v_{rd_{SMC}}$ and $v_{rq_{SMC}}$ terms. Despite this, the robustness of the overall control algorithm in (21) and (22) is not compromised, since such robustness rests on its SMC terms.

Accordingly, in order to deal with the impact of uncertainties and disturbances, the 1-SMC discontinuous terms in (19) and (20) are calculated as

$$u_{d_{SMC}} = K_d\,\mathrm{sign}(s_d) \tag{31}$$

$$u_{q_{SMC}} = K_q\,\mathrm{sign}(s_q), \tag{32}$$

where both K_d and K_q are positive constants which must be selected sufficiently high to reach —or restore— and preserve the sliding regime even in presence of disturbances and uncertainties, both parametric and unstructured. The following subsection —Section II-C— is devoted to prove the latter, as well as to show that, if the closed-loop state trajectories are not on the sliding surface, they will hit it in finite time provided that K_d and K_q are properly chosen.

As reasoned above, once the sliding regime is achieved, the voltage errors will become null. This implies that, rather than vanishing to zero following certain dynamics, the voltage errors will theoretically be equal to zero, showing no dynamics, while in the sliding regime. This conclusion can be corroborated by considering that the closed-loop dynamics in the sliding regime coincide with those resulting from applying only equivalent control in absence of uncertainties and disturbances [38]. Indeed, substitution of (25) and (26) into, respectively, (10) and (11) also leads to $v_{sd} = v^*_{sd}$ and $v_{sq} = v^*_{sq}$ when all perturbations are neglected.

It should also be noted that the $v_{rd_{SMC}}$ and $v_{rq_{SMC}}$ control terms in (21) and (22), computed as

$$v_{rd_{SMC}} = K_d\int_0^t \mathrm{sign}\left(s_d(\tau)\right)d\tau \tag{33}$$

$$v_{rq_{SMC}} = K_q\int_0^t \mathrm{sign}\left(s_q(\tau)\right)d\tau \tag{34}$$

by time integration of the 1-SMC terms in (31) and (32), are no longer discontinuous. This is a key feature of the proposed solution, as it prevents chattering without the need to take any additional specific measure.

C. Analysis of stability and robustness

Aiming to achieve the convergence of s_d and s_q to zero in the face of disturbances and uncertainties —both parametric and unstructured—, and hence prove the stability and robustness of the resulting closed-loop system, the following positive-definite Lyapunov function is taken as starting point:

$$V = \frac{1}{2}\left(s_d^2 + s_q^2\right), \tag{35}$$

whose time derivative must be negative-definite; that is,

$$\dot{V} = s_d\dot{s}_d + s_q\dot{s}_q < 0. \tag{36}$$

Replacing the designed control law —resulting from substitution of (23)-(24) and (31)-(32) into (19)-(20)— in (15) and (16), the state equations expressed as a function of the switching variables are derived as follows:

$$\dot{s}_d = h_d - \frac{L_m}{L_r}K_d\,\mathrm{sign}\,(s_d) \tag{37}$$

$$\dot{s}_q = h_q - \frac{L_m}{L_r}K_q\,\mathrm{sign}\,(s_q)\,, \tag{38}$$

where the h_d and h_q perturbation functions turn out to be

$$h_d = \varepsilon\dot{v}^*_{sd} + \frac{L_m}{L_r}\left[\Delta R_r\dot{i}_{rd} + \Delta L_r\left(\dot{\omega}_r i_{rq} + \omega_r\dot{i}_{rq}\right)\right] + m_d \tag{39}$$

$$h_q = \varepsilon\dot{v}^*_{sq} + \frac{L_m}{L_r}\left[\Delta R_r\dot{i}_{rq} - \Delta L_r\left(\dot{\omega}_r i_{rd} + \omega_r\dot{i}_{rd}\right)\right] + m_q, \tag{40}$$

with $\varepsilon = 1 - {}^{(L_m\hat{L}_r)}/_{(\hat{L}_m L_r)}$. Note that, in absence of parameter mismatch, only the effects of lumped disturbances and unmodeled dynamics, m_d and m_q, are present in perturbation functions h_d and h_q.

If $K_d = K_q = K$ is selected for simplicity, substitution of (37) and (38) into (36) yields the following condition:

$$\dot{V} = \underbrace{h_d s_d + h_q s_q}_{a} - \underbrace{\frac{L_m}{L_r}K\left(|s_d| + |s_q|\right)}_{b} < 0, \tag{41}$$

whose all-case fulfillment requires that $b > |a|$.

Considering the worst-case scenario, in which a would reach the highest possible value —its two addends being positive—, the above condition becomes

$$\dot{V} \leq |h_d||s_d| + |h_q||s_q| - \frac{L_m}{L_r}K\left(|s_d| + |s_q|\right) < 0. \tag{42}$$

Assuming that perturbation functions h_d and h_q are upper bounded so that $|h_d| < H_d$ and $|h_q| < H_q$, where H_d and H_q are positive constants, and defining $H = \max\left(H_d, H_q\right)$, (42) leads to

$$\dot{V} \leq -\underbrace{\left(\frac{L_m}{L_r}K - H\right)}_{\eta}\left(|s_d| + |s_q|\right) < 0. \tag{43}$$

From this expression, it can be concluded that both s_d and s_q will converge to zero despite the presence of disturbances and uncertainties, both parametric and unmodeled, if K is selected high enough to satisfy $\eta > 0$, hence demanding that

$$K > \frac{L_r}{L_m}H. \tag{44}$$

On the other hand, (43) also allows estimating an upper bound for the time required to reach the sliding regime, T_{reach}. Indeed, if the triangle inequality and (35) are applied, the following majorant expression is obtained

$$\dot{V} \leq -\eta\left(|s_d| + |s_q|\right) \leq -\eta\sqrt{s_d^2 + s_q^2} = -\eta\sqrt{2V}, \tag{45}$$

which, integrated in time for an arbitrary initial condition $V(0) > 0$, yields

$$V \leq \left(-\frac{\eta}{2}t + \sqrt{V(0)}\right)^2. \tag{46}$$

Accordingly, considering the expressions for V and η provided in (35) and (43), the maximum reaching time needed to achieve the sliding regime, $V(t_{reach}) = 0$, can be estimated as

$$t_{reach} \leq T_{reach} = \frac{\sqrt{2}}{\frac{L_m}{L_r}K - H}\sqrt{s_d^2(0) + s_q^2(0)}, \tag{47}$$

where $s_d(0)$ and $s_q(0)$ should be interpreted not only as the initial values of the switching variables, but also as the maximum values they reach when a disturbance takes the closed-loop system out of the sliding regime. Note that the higher the deviation from zero of s_d and s_q, the longer the reaching time required. Likewise, if H increases, so does the reaching time, whereas a faster approach to the sliding surface is obtained by increasing K.

D. Rotor positioning

Since the three-phase components of the voltage to be applied to the rotor are obtained by the combined Park's and inverse Clarke's transformation of v_{rd} and v_{rq}, the electrical position of the rotor needs to be known. Consequently, this subsection is devoted to briefly describe a method for rotor positioning.

If an absolute encoder was used to measure rotor position, this task would not be necessary. However, in the case of using an incremental encoder —probably the most common practice—, which only reports changes with respect to an initial position, some simple calculations are required to determine the correct rotor position from the information provided by the encoder.

Fig. 1 represents the actual rotor electrical position, θ_r, and that derived from the encoder, θ_{re}, together with their respective associated reference frames, both of which rotate at the same ω_r speed. It is evident that θ_r could be straightforwardly deduced from θ_{re} as

$$\theta_r = \theta_{re} + \theta_o, \tag{48}$$

if the constant θ_o offset angle was known.

As depicted in Fig. 1, the actual rotor angular position can be estimated as follows:

$$\hat{\theta}_r = \delta - \gamma, \tag{49}$$

where $\delta = \arctan(i_{rq}/i_{rd})$ and $\gamma = \arctan(i_{r\beta}/i_{r\alpha})$. According to (5), the stationary-frame rotor current components may be derived by time integration of those of the stator voltage as

$$i_{rd} = \frac{1}{L_m}\int_0^t v_{sd}(\tau)d\tau;\ i_{rq} = \frac{1}{L_m}\int_0^t v_{sq}(\tau)d\tau, \tag{50}$$

which, together with (49), leads to the non-parameter-dependent estimation of the rotor position given next:

$$\hat{\theta}_r = \arctan\left(\frac{\int_0^t v_{sq}(\tau)d\tau}{\int_0^t v_{sd}(\tau)d\tau}\right) - \arctan\left(\frac{i_{r\beta}}{i_{r\alpha}}\right). \tag{51}$$

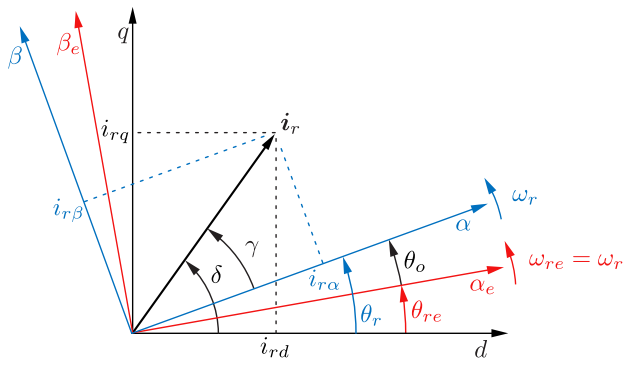

Fig. 1. Direct- and quadrature-axis components of the $\boldsymbol{i}_r$ space-vector, according to both the rotor and stationary reference frames.

Given that all the expressions on which the foregoing reasoning is based are general for DFIGs whose stator is open, the results derived from such reasoning remain valid even if the rotor current and the induced stator voltage exhibit harmonic distortion and/or imbalance. This suggests that rotor positioning may be conducted simultaneously with the earlier part of the synchronization process, during which θ_r may be approximated by the $\hat{\theta}_r$ given in (51), while θ_o is determined as follows:

$$\theta_o = \hat{\theta}_r - \theta_{re}. \tag{52}$$

Once the θ_o thus computed is assumed to have practically converged to its actual value —typically a few grid cycles later—, its calculation can cease to be updated, hence concluding the rotor positioning. From that instant on, θ_r should be derived as in (48).

E. Functional diagram of the control strategy

Fig. 2 depicts the functional diagram of the proposed control scheme, which should be implemented up-down and from the rearmost layer —labeled as "1st Step" in its bottom left-hand corner— to the frontmost one —labeled as "3rd Step". Likewise, it must also be assumed that any parameter or variable used/calculated in a given layer will be accessible by the layers inside.

The displayed control algorithm is valid regardless of whether rotor positioning is running or not, with only two differences to be considered. As evidenced by the "if-else" statement within the layer named "1st Step", one consists in the additional calculations in (51) and (52) required to compute the θ_o offset angle while rotor positioning is active. The other concerns the θ angle involved in the Park's transform represented as "$e^{j\theta}$" in the "3rd Step". According to the above-cited "if-else" statement, θ equals the $\hat{\theta}_r$ estimated as in (51) when rotor positioning runs simultaneously to synchronization. In contrast, it equals the θ_r derived as in (48) after rotor positioning has concluded and θ_o is assumed to have converged to its actual value.

It is also worth highlighting that, as represented in the layer labeled as "2nd Step", rather than forcing $v_{sd}^* = v_{gd}$ and $v_{sq}^* = v_{gq}$ from the beginning, v_{sd}^* and v_{sq}^* are respectively ramped up from zero to the v_{gd} and v_{gq} grid voltage components to be tracked. Abrupt changes in the rotor current are thus avoided. Otherwise, the induced voltage would uncontrollably increase [23], as dictated by (5) and already noted in Section II-A.

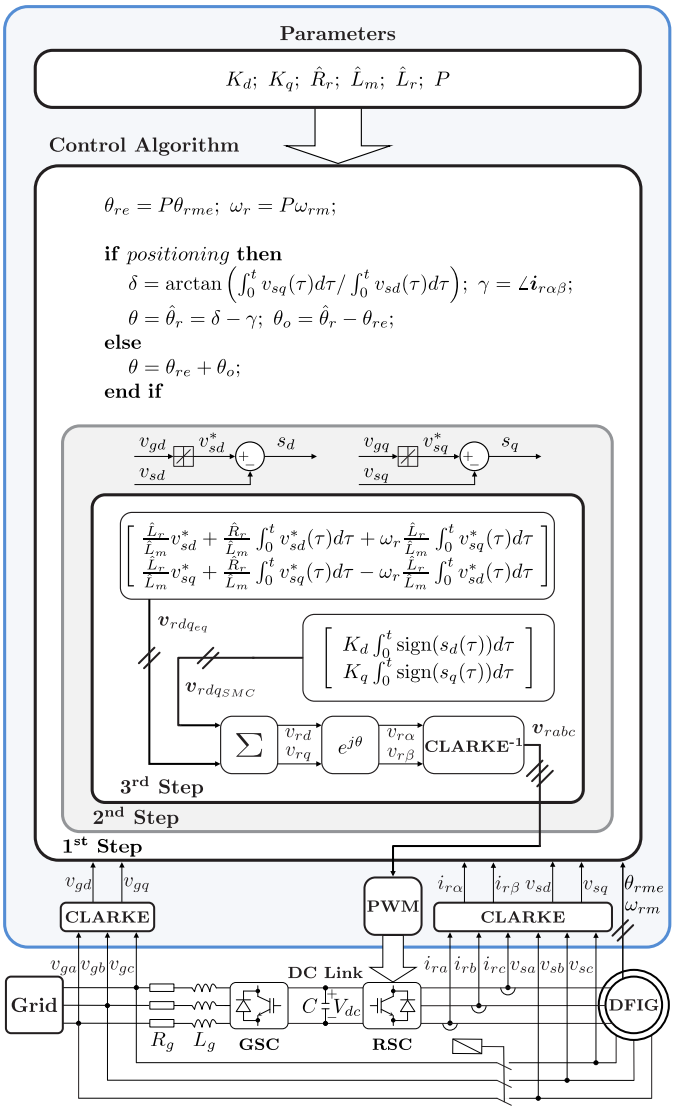

Fig. 2. Functional diagram of the proposed control strategy.

Finally, Fig. 2 evidences that the proposed control algorithm is PLL-less. Indeed, only knowledge of the stationary-frame v_{gd} and v_{gq} grid voltage components is required to achieve grid synchronization, for which a Clarke's transform of the three-phase grid voltage is sufficient.

III. Simulation Results

With the intention of validating the proposed strategy in simulation, a model consisting of a 2-MW DFIG —whose electrical parameters are provided in Table I [39]— and its overall control system was built in MATLAB/Simulink. In particular, the three-phase model of the generator was implemented by means of a C MEX-type Simulink S-function block, in which the "quadrature-phase slip-ring" space-vector model [35] was programmed for both the open stator and grid-connected operating modes. With regard to the back-to-back converter, it was represented by an average-value model

to unambiguously identify the chattering due to the SMC strategy, and not to confuse it with that coming from the commutation of the converter transistors.

TABLE I
PARAMETERS OF THE 2-MW DFIG + DC BUS + GRID FILTER SET

Parameter	Value	Parameter	Value
$V_{g\,rms}(f)$	$\frac{690}{\sqrt{3}}$ V(50 Hz)	R_{r0}	2.9 mΩ
n	0.333	L_{lr}	83.369 μH
P	2	L_{r0}=L_{lr}+$\frac{L_{m0}}{n}$	7.591 mH
L_{m0}	2.5 mH	V_{dc}	1200 V
R_{s0}	2.6 mΩ	C	16 mF
L_{ls}	77.306 μH	R_g	0.0 mΩ
L_{s0}=L_{ls}+nL_{m0}	909.806 μH	L_g	250 μH

The RSC control algorithm for DFIG synchronization described throughout Sections II-B and II-D, as well as depicted in Fig. 2, was also realized making use of the C MEX S-function tool. With the aim of getting closer to the final implementation of such control algorithm, which commonly involves the use of a digital embedded system, it was discretized via Tustin's bilinear approximation, being the selected sample time $T_s = 50$ μs. In addition, the gains corresponding to the 1-SMC terms of the control scheme, $K_d = K_q = 1920$ V/s, were heuristically tuned to fulfill (44).

Although the grid-connected operation of the DFIG is outside the scope of this paper, the RSC control scheme for that operating regime was also programmed in the same S-function containing the synchronization algorithm. The only purpose of doing so was to assess the quality of the connection immediately following a synchronization guided by the latter. Details on the control strategy implemented for grid-connected operation can be found in a previous contribution by the authors [36]. Concerning the grid-side converter (GSC), its control scheme was also adopted from [36] and programmed in a third S-function. The whole model was executed adopting the ode4 (Runge-Kutta) solver with a fixed step size of 50 μs, sufficient to properly represent the DFIG dynamics.

A test consisting in the sequence of operation modes reflected in Table II was designed, in which rotor positioning was active during the entire synchronization ramp up. The test was driven by a state machine programmed in a fourth and last S-function. In order to analyze the behavior of the algorithm when subject to a realistically varying rotational speed, during the test, the DFIG was forced to rotate at the mechanical speed reflected in Fig. 3. Such reference speed profile was previously obtained, as a result of feeding the simulation model of a 2-MW wind turbine with real wind speed data.

TABLE II
STAGES OF THE DESIGNED TEST

Time interval (s)	Operation mode
0.0–0.5	Synchronization ramp up (Positioning on)
0.5–2.5	Synchronization (Positioning off)
2.5–3.5	Connected to the grid at zero power

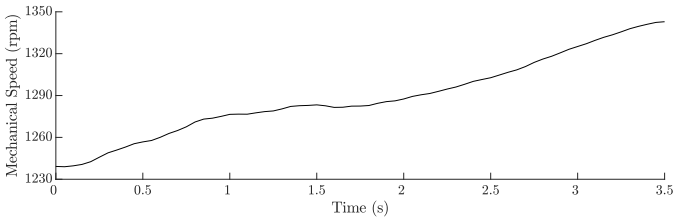

Fig. 3. Rotational speed of the DFIG during the test.

A. Simulation case study 1: Performance under disturbed grid

The grid voltage was subject to harmonic distortion during all this first simulation case study. Specifically, it exhibited 6% and 5%, respectively, of the 5$^{\text{th}}$ and 7$^{\text{th}}$ order harmonics, resulting in a total harmonic distortion (THD) of 7.81%. From second 1.5 onward, a two-phase E-type imbalance of 15% depth was also incorporated. Fig. 4(a) shows the grid and stator three-phase voltages throughout the three stages of the test.

Although rotor positioning is ongoing during the synchronization ramp up, the details in Fig. 4(b) and 4(c) —where only phase b is displayed for the sake of clarity— reveal that the stator voltage tracks its reference from the very beginning of the ramp, as both three-phase signals are almost indistinguishable. This points to a superior dynamic response of the synchronization control-loop, as well as to a satisfactory performance of the rotor positioning method practically from the start, despite the harmonic distortion affecting the grid voltage. Rotor positioning will be discussed in more detail in the next simulation case study.

Afterwards, with the synchronization stage still in progress, the two-phase imbalance occurs at second 1.5, as detailed in Fig. 4(d). Despite this, it is observed that the stator voltage tracks that of the grid with virtually no transient, corroborating the high-performance dynamic response expected for the resulting closed-loop system. Note that the stator and grid voltages are fully synchronized and thus overlap almost perfectly, leading to the smooth connection shown at second 2.5 in Fig. 4(e). As foreseen in Section II-B, no chatter is observable in the stator voltages displayed in Fig. 4(b), 4(c), 4(d) and 4(e). Finally, Fig. 4(f) and 4(g) are included with the sole purpose of illustrating the absence of peaks in the stator and rotor currents, respectively, when connecting the former to the grid at zero power. Note also that the harmonic distortion present in the rotor current of Fig. 4(g) is that strictly required to induce a replica of the unbalanced and harmonically distorted grid voltage at the open stator terminals.

B. Simulation case study 2: Robustness under disturbed grid

This test was conceived with the aim of evaluating the robustness of the proposed control strategy against both parametric uncertainty and common disturbances of different nature.

To that end, several parameters of the DFIG simulation model were modified, whereas the control algorithm was deliberately unaware of such changes. In particular, considering that continuous operation of the DFIG could lead to variations

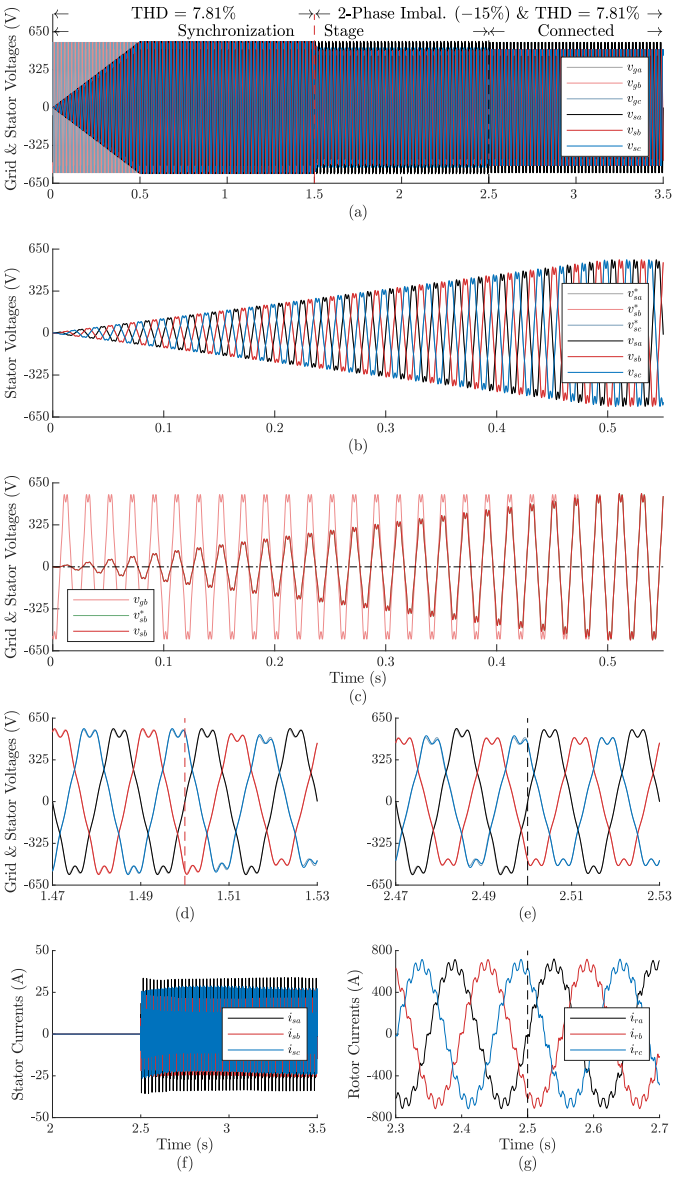

Fig. 4. Simulation case study 1: Performance under disturbed grid. (a) Grid and stator voltages. (b) Stator voltages at the beginning of the synchronization stage. (c) Grid and stator voltages of phase b at the beginning of the synchronization stage. (d) Detail of the imbalance's incidence. (e) Detail of the synchronization and connection stages. (f) Stator currents before/after connection. (g) Rotor currents before/after connection.

in its parameters, the magnetizing inductance was decreased by 30% with respect to its L_{m0} nominal value —and, therefore, so were L_s and L_r in their corresponding proportions; see Table III. In contrast, the values of R_s and R_r were increased by 100% with respect to R_{s0} and R_{r0}.

On the other hand, in addition to the disturbance caused by the varying rotor speed profile, a grid frequency fluctuation of $\Delta f = \pm 2.5$ Hz was also incorporated. Furthermore, unlike in the preceding case study, the grid voltage remained unbalanced and harmonically distorted during this entire simulation trial, the imbalance and harmonic content being coincident with those applied in Section III-A.

In addition to the grid and stator voltages corresponding to the whole test, Fig. 5(a) shows the sinusoidal variation

TABLE III
PARAMETERS ADOPTED IN SIMULATION CASE STUDY 2

DFIG model	**Overall control system**
$L_m = 0.7L_{m0}$	$\hat{L}_m = L_{m0}$
$R_r = 2R_{r0}$	$\hat{R}_r = R_{r0}$
$L_r = L_{lr} + \frac{0.7L_{m0}}{n}$	$\hat{L}_r = L_{lr} + \frac{L_{m0}}{n}$
$R_s = 2R_{s0}$	$\hat{R}_s = R_{s0}$ (Unused in synchronization)
$L_s = L_{ls} + n0.7L_{m0}$	$\hat{L}_s = L_{ls} + nL_{m0}$ (Unused in synchronization)

undergone by the grid frequency, which covers the range from 47.5 to 52.5 Hz throughout the entire test. Neither the variable rotor speed nor the fact that the grid voltage is subject to simultaneous imbalance, harmonic distortion and fluctuating frequency prevent the computation of θ_o from being performed correctly almost from the beginning of the test —see Fig. 5(b). Indeed, as illustrated in Fig. 5(c), the error between the actual and estimated angular positions becomes lower than 0.5° after only a few grid cycles. It is also worth noting that, being parameter-independent, the rotor positioning process is unaffected by the substantial parameter mismatch reproduced.

Again, Fig. 5(d) and 5(e) show that the induced three-phase stator voltage practically matches its reference from the start of the synchronization stage, which is another evidence of the outstanding dynamic response achieved by applying the presented synchronization algorithm. Accordingly, both synchronization and grid connection are satisfactorily performed despite the introduced parametric deviations and disturbances, as endorsed by Fig. 5(f), 5(g), 5(h) and 5(i).

The absence of chatter in the induced stator voltage is again confirmed in Fig. 5(d), 5(e), 5(f) and 5(g). Note that, as a consequence of having reduced the value of L_m, the amplitude of the rotor current in Fig. 5(i) has significantly increased, compared to that of the previous case study, in order to induce the same voltage amplitude at the stator terminals. Likewise, given that the grid frequency exceeds its nominal value around the connection instant —see Fig. 5(a)—, the frequency of the rotor current in Fig. 5(i) is considerably higher than that in Fig. 4(g).

IV. EXPERIMENTAL VALIDATION

With the purpose of experimentally validating the proposed solution, rapid control prototyping (RCP) of the same S-function-based global control system developed for simulation was performed, via the OP5600 platform by Opal-RT, over the 7-kW DFIG test bench shown in Fig. 6(a). The rotor terminals of the DFIG, whose electrical parameters are collected in Table IV, were connected to the SKiiP 132 GD 120–318 CTV three-phase two-level voltage source converter manufactured by Semikron. Moreover, the DFIG was driven by a 15-kW armature-controlled DC motor, whose rotational speed was commanded by means of a commercial adjustable speed drive to fit the profile shown in Fig. 3. Thereby, the disturbance due to wind speed variability was represented in all the three experimental case studies addressed hereafter.

Given that the rated power of the laboratory-scale DFIG is considerably lower than that of the simulation model, its

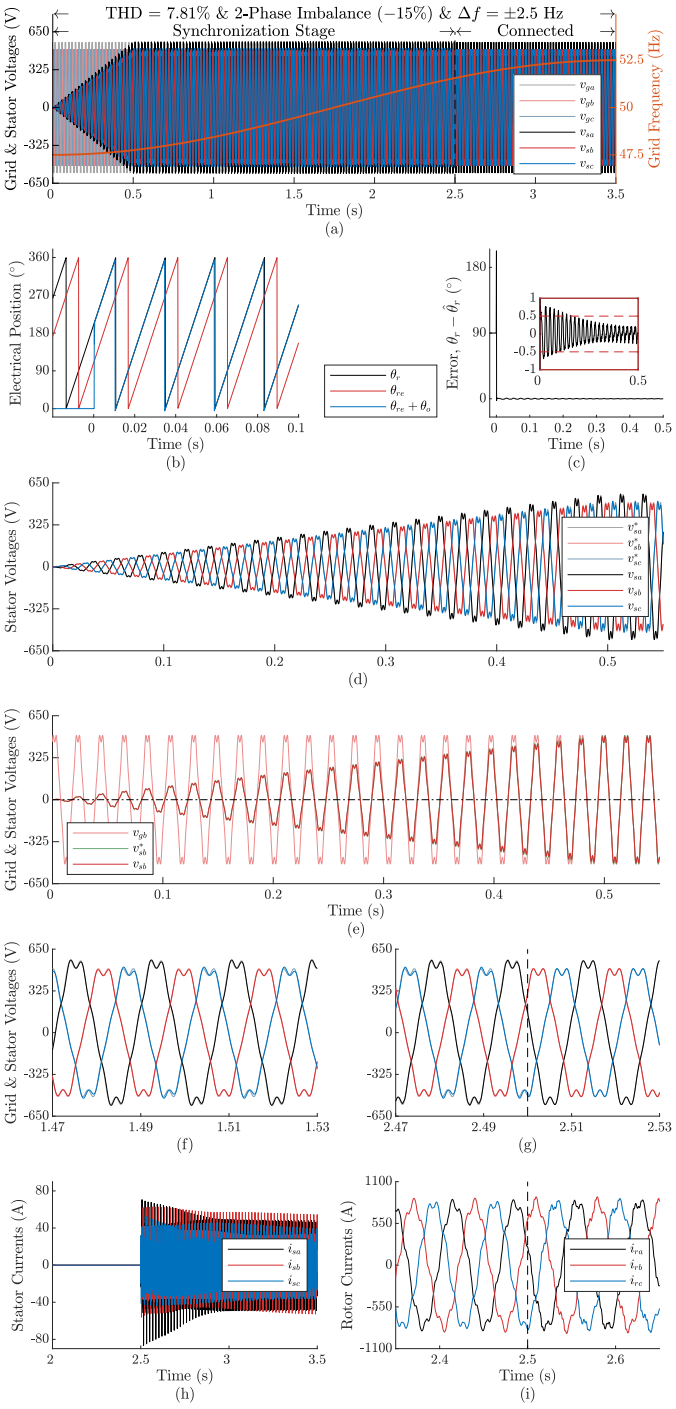

Fig. 5. Simulation case study 2: Robustness test. (a) Grid frequency, and grid and stator voltages. (b) Start of the calculation for rotor positioning. (c) Position error, $\theta_r - \hat{\theta}_r$. (d) Stator voltages at the beginning of the synchronization stage. (e) Grid and stator voltages of phase b at the beginning of the synchronization stage. (f) Detail of the synchronization stage. (g) Detail of the synchronization and connection stages. (h) Stator currents before/after connection. (i) Rotor currents before/after connection.

parameters are different, thus making it necessary to re-tune the gains of the SMC terms to $K_d = K_q = 2600$ V/s. However, the sample time remained the same —$T_s = 50$ μs. Concerning the rotor voltage computed by the control algorithm, it acted as a three-phase modulating signal for the triangular carrier PWM driving the RSC at a switching

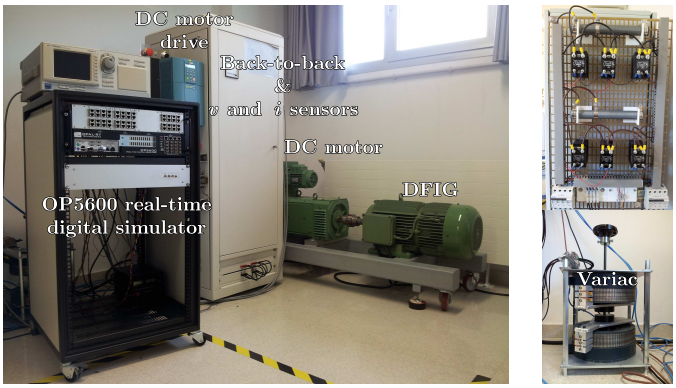

(a) (b)

Fig. 6. Experimental rig. (a) General view of the test bench. (b) Equipment reproducing controlled two-phase voltage imbalances.

TABLE IV
PARAMETERS OF THE 7-KW DFIG + DC BUS + GRID FILTER SET

Parameter	Value	Parameter	Value
$V_{g\,rms}(f)$	$\frac{380}{\sqrt{3}}$ V(50 Hz)	R_{r0}	145.8541 mΩ
n	2.001	L_{lr}	1.2138 mH
P	2	L_{r0}=L_{lr}+$\frac{L_{m0}}{n}$	20.045 mH
L_{m0}	37.6812 mH	V_{dc}	125 V
R_{s0}	370 mΩ	C	9.4 mF
L_{ls}	4.86 mH	R_g	16 mΩ
L_{s0}=L_{ls}+nL_{m0}	80.2601 mH	L_g	2 mH

frequency of 10 kHz, which is a value commonly adopted for lab-scale converters of similar power ratings [10], [23], [31]. Notice that the sampling frequency was thus set to twice the switching frequency, since such proportion between those two magnitudes is often the default in commercially available programmable digital devices providing built-in PWM blocks. Furthermore, in order to avoid the phenomenon known as drift [40], each integral in the equivalent control terms (29) and (30), as well as the two computed in (51) during rotor positioning, were replaced by band-pass filters with upper and lower cut-off frequencies of 0.5 Hz. The three stages of the experimental tests presented below coincide with those reflected in Table II.

Finally, it is important to note that the amplitude of the induced stator voltage is obviously small at the beginning of rotor positioning. In practice, if the measurement of such magnitude is also noise-polluted, the calculation in (51) may lead to deviations in the estimated rotor angular position. Consequently, to effectively start up the synchronization process, v_{sd} and v_{sq} may respectively be approximated by v^*_{sd} and v^*_{sq} in (51) until the magnitude of the stator voltage reaches a certain threshold fraction of the grid voltage magnitude. Such threshold was set to 30% in the experiments whose results are discussed in Sections IV-A and IV-B.

A. Experimental case study 1: Performance under disturbed grid

As displayed in Fig. 7(a), the grid voltage of the laboratory presented a THD of around 3.8% during this experimental test

aimed at validating the performance of the proposed control strategy. In particular, the 3rd, 5th and 7th harmonic components were, respectively, of 2.7%, 2.9% and 0.9%. In addition, as of second 1.5, the same two-phase E-type imbalance applied in Section III-A was reproduced using a low-cost device similar to that described in [41] —see Fig. 6(b).

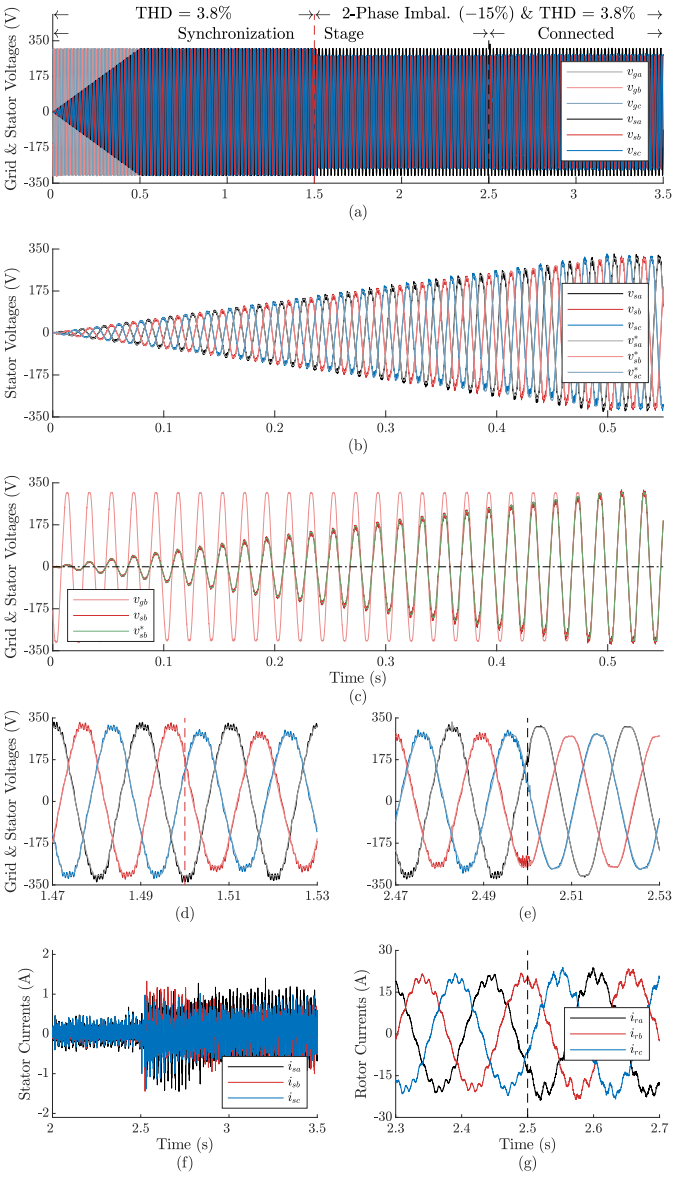

Fig. 7. Experimental case study 1: Performance under disturbed grid. (a) Grid and stator voltages. (b) Stator voltages at the beginning of the synchronization stage. (c) Grid and stator voltages of phase b at the beginning of the synchronization stage. (d) Detail of the imbalance's incidence. (e) Detail of the synchronization and connection stages. (f) Stator currents before/after connection. (g) Rotor currents before/after connection.

Analogously to the simulation results commented on in Section III, Fig. 7(b) and 7(c) vindicate the agile rotor positioning achieved, as well as the outstanding dynamic response conferred by the proposed synchronization algorithm, as the stator voltage is overlapped to its reference almost perfectly from the very beginning of the synchronization ramp up. Such high-performance dynamics are also corroborated in Fig. 7(d), which evidences the lack of transient following the imbalance introduced at second 1.5. Finally, the smoothness of the grid connection performed at second 2.5 is supported by Fig. 7(e), 7(f) and 7(g).

B. Experimental case study 2: Robustness under disturbed grid

This test is intended to assess the robustness of the control scheme not only under the disturbance due to wind speed variability, but also against substantial parameter mismatch. Given that the DFIG parameters can obviously not be changed at will as in simulation, the values of all the parameters used within the overall control algorithm were deliberately modified as reflected in Table V. Assuming that the actual values of those parameters practically coincided with their respective nominal values, a deviation equivalent to that applied in simulation —refer to Table III— was thus represented. As displayed in Fig. 8(a), the grid voltage was subject to virtually the same harmonic distortion reported in the preceding case study, whereas the same two-phase imbalance was present between seconds 0 and 1, as well as from second 2 onward. In contrast, the grid was kept balanced between seconds 1 and 2.

TABLE V
PARAMETERS ADOPTED FOR EXPERIMENTAL CASE STUDY 2

DFIG prototype	**Overall control system**
$L_m \simeq L_{m0}$	$\hat{L}_m = \frac{L_{m0}}{0.7}$
$R_r \simeq R_{r0}$	$\hat{R}_r = \frac{R_{r0}}{2}$
$L_r \simeq L_{lr} + \frac{L_{m0}}{n}$	$\hat{L}_r = L_{lr} + \frac{L_{m0}}{0.7n}$
$R_s \simeq R_{s0}$	$\hat{R}_s = \frac{R_{s0}}{2}$ (Unused in synchronization)
$L_s \simeq L_{ls} + nL_{m0}$	$\hat{L}_s = L_{ls} + n\frac{L_{m0}}{0.7}$ (Unused in synchronization)

As shown in Fig. 8(b) and 8(c), once again the induced stator voltage tracks its three-phase reference from the start of the synchronization ramp up. This proves not only that the agile and satisfactory operation of the rotor positioning method remains unaffected by the grid voltage imbalance, but also that the high-performance dynamic response exhibited by the synchronization control-loop is retained under considerable parameter mismatch. The latter is even further substantiated by the virtual absence of transients following the clearance and reappearance of the voltage imbalance occurring, respectively, at seconds 1 and 2, as evidenced by the left and middle sections of Fig. 8(d). Furthermore, Fig. 8(d), 8(e), and 8(f) support both the successful completion of synchronization and the subsequent smooth grid connection, despite the significant deviations affecting the values of the DFIG parameters used within the control algorithm.

In the experiments presented so far, the instant of connection was intentionally delayed up to 2.5 s so as to better assess the robustness, stability and dynamic behavior of the synchronization algorithm in presence of varying rotational speed and/or grid frequency, or even under imbalances that might arise or be removed with synchronization still in progress. Nevertheless, it is important to note that the duration of the synchronization stage can be significantly shortened without detriment to the behavior of the control system.

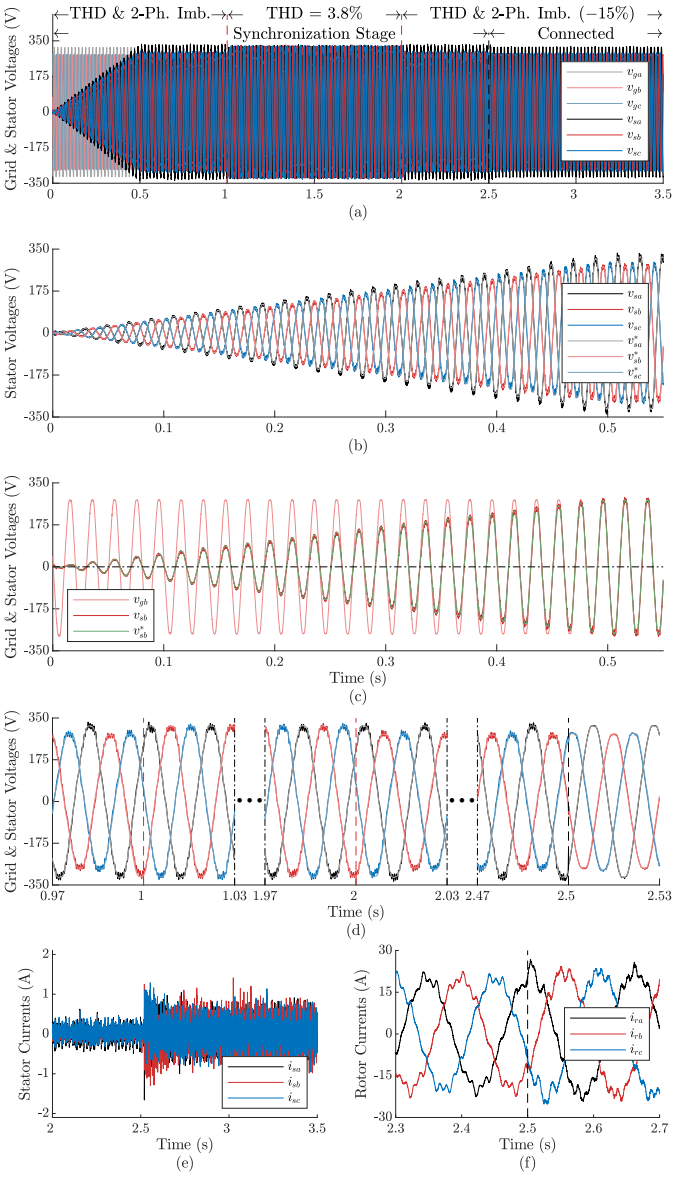

Fig. 8. Experimental case study 2.1: Robustness test. (a) Grid and stator voltages. (b) Stator voltages at the beginning of the synchronization stage. (c) Grid and stator voltages of phase b at the beginning of the synchronization stage. (d) Incidence of the imbalance clearance and reappearance during synchronization, and detail of grid connection. (e) Stator currents before/after connection. (f) Rotor currents before/after connection.

With the aim of supporting this assertion, a test was carried out that reproduced the same grid voltage disturbance, parameter mismatch and speed profile of the immediately preceding one, but adjusting the ramp up time to 0.1 s. After the rise, the synchronization stage is held for approximately another 0.1 s, as displayed in Fig. 9(a), simply to demonstrate that the induced stator voltage is stable and synchronized with that of the grid. Nonetheless, the connection could be made directly once the end of the ramp has been reached. Fig. 9(b), 9(c) and 9(d) again confirm the excellent tracking of the grid voltages and the smoothness of the performed connection.

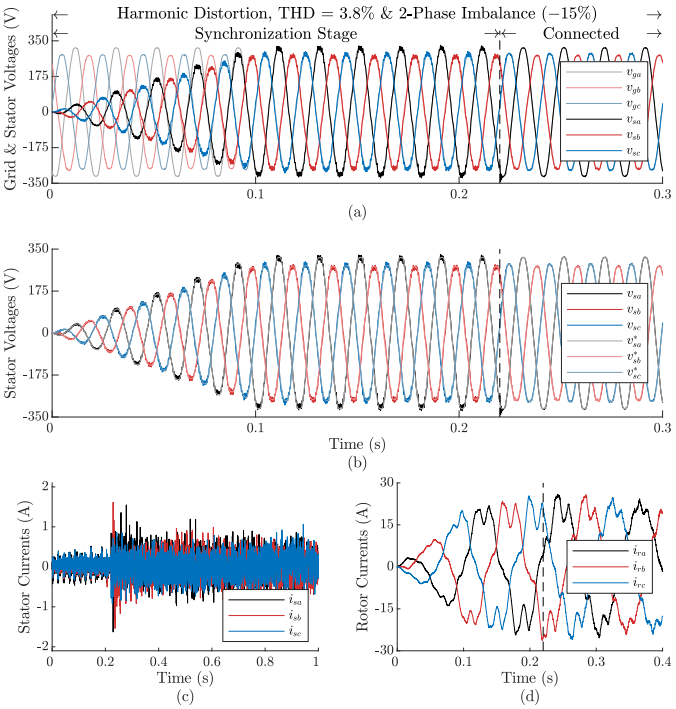

Fig. 9. Experimental case study 2.2: Robustness test under rapid synchronization. (a) Grid and stator voltages. (b) Stator voltages. (c) Stator currents before/after connection. (d) Rotor currents before/after connection.

C. *Experimental case study 3: Performance under faulty grid*

Given that the low-cost equipment of Fig. 6(b) does not allow harmonic content to be incorporated into the grid voltage at will, the harmonic distortion in the three previous experiments was naturally present in the laboratory housing the test bench.

Nonetheless, a failure suffered by the power grid in the area where the laboratory is located made it possible to perform a test under severe harmonic distortion. Indeed, during one of the experiments aimed at evaluating the grid synchronization achieved under the two-phase E-type imbalance, the THD of the grid rose accidentally to 10.2%, the 3$^{\text{rd}}$, 5$^{\text{th}}$ and 7$^{\text{th}}$ harmonic components being of 2%, 8.86% and 4.3%, respectively. Furthermore, the failure also caused an overvoltage that increased the grid voltage by 10.7% —see Fig. 10(a).

It should be clarified that, as this was one of the earliest tests performed to analyze the feasibility of the proposed strategy, the rotor positioning method was not yet fully optimized and integrated into the synchronization algorithm. As a consequence, the dynamics exhibited in the initial ramp differ from those shown in the experimental tests discussed above.

In contrast, the synchronization controller was already developed as presented in Section II-B. In this regard, Fig. 10(b) and 10(c) substantiate that, despite the three aforementioned demanding simultaneous disturbances and the manifest asymmetry of the grid voltage waveform faced by the control system, it is still able to synchronize the stator voltage with that of the grid, and properly connect the DFIG to the grid even at the most adverse instant —when two of the three phases reach their respective peak values. A closer look at

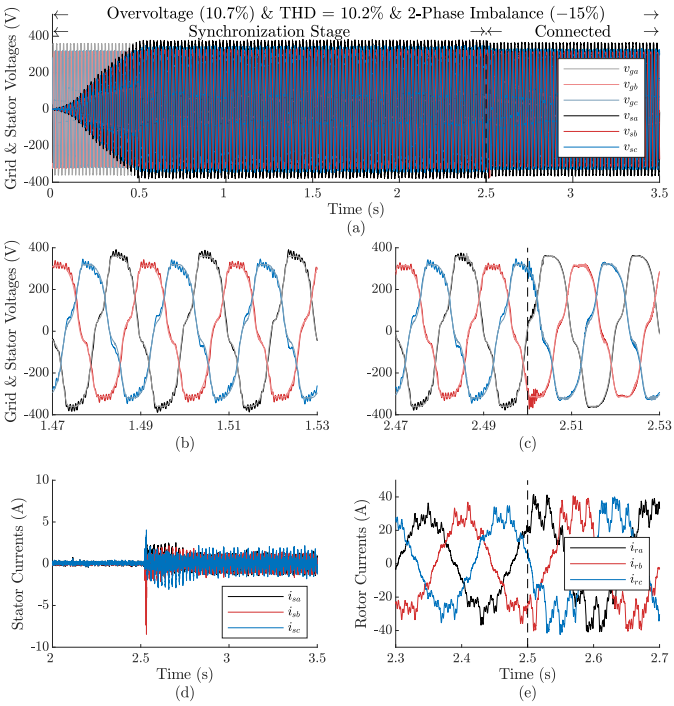

Fig. 10. Experimental case study 3: Performance under faulty grid. (a) Grid and stator voltages. (b) Detail of the synchronization stage. (c) Detail of the synchronization and connection stages. (d) Stator currents before/after connection. (e) Rotor currents before/after connection.

Fig. 10(d) reveals the peak experienced by the stator current immediately after connection. However, it is well below the rated peak current of 16 A, representing its 52.8%.

As expected, Fig. 10(e) confirms that the amplitude of the rotor current has risen above those in Fig. 7(g), 8(g) and 9(d), since the voltage induced in the stator needs to be increased to track the overvoltage in the grid.

V. Conclusion

Considering not only the high robustness against disturbances and uncertainties —both parametric and unstructured— provided by the variable-structure control methodology, but also the rapid responsiveness it confers, a PLL-less and naturally chatter-free SMC-based algorithm has been put forward in order to deal with the DFIG synchronization task in the face of permanently disturbed grid voltages —simultaneously unbalanced and harmonically distorted.

Given the trajectory tracking capability inherent to such control technique, the solution has been designed according to the stationary reference frame, which makes it possible to dispense with the extraction of positive- and negative-sequences and harmonic components. In addition, a single control loop per voltage component is implemented, for which only one gain needs to be tuned. A convergence proof has shown that proper selection of such gain guarantees finite-time achievement and maintenance of the sliding regime under both uncertainties and disturbances.

In order to analyze the validity of the control algorithm on generators of different power ratings, simulation and RCP tests have respectively been carried out on a 2-MW DFIG model and on a 7-kW DFIG test bench. In all cases, a variable rotor speed profile caused by a plausibly varying wind speed has been reproduced.

Both simulation and experimental results corroborate that the proposed solution is able to successfully position the rotor and synchronize the DFIG to grids subject to simultaneous imbalances and harmonic distortion. In particular, such solution has proven to be effective in the face of concurrent two-phase imbalances of 15% and harmonic distortions of THDs up to 10.2%, and even under an overvoltage of 10.7% accidentally arisen during one of the experimental case studies. Moreover, its robustness has been substantiated in presence of simultaneous 30% and 100% mismatches, respectively, in the DFIG inductances and resistances, as well as under common disturbances, such as a variable rotational speed caused by a realistic wind speed profile and a ± 2.5-Hz fluctuation of the grid frequency around its rated value.

Furthermore, simulation and experimentation also confirm that the resulting closed-loop synchronization system exhibits a high-performance dynamic response, since, in addition to driving the induced stator voltage to track its reference from the very beginning of the synchronization process, it shows virtually no transients following the imbalances introduced or removed during synchronization.

In summary, all the aforementioned aspects contribute to making the presented control strategy highly industrializable.

Acknowledgment

The authors would like to thank Imanol Bardají for his valuable assistance during commissioning of the experimental rig, as well as Prof. Jorge A. Solsona and Prof. María Calzada-Pérez for their helpful advice.

References

[1] International Renewable Energy Agency (IRENA). (2021) Statistics time series. [Online]. Available: https://www.irena.org/Statistics/View-Data-by-Topic/Capacity-and-Generation/Statistics-Time-Series

[2] P. Chimurkar and P. Kothavade, "A review of different power converter topologies for PMSGs wind turbine," in *Proc. 11th Int. Conf. ICCES*, 2016, pp. 1–6.

[3] C. Vázquez-Hernández, T. Telsnig, and A. Villalba-Pradas, "JRC Wind Energy Status Report – 2016 Edition," European Union. Joint Research Centre. Directorate for Energy, Transport and Climate, Tech. Rep., 2017.

[4] Vestas. (2021) Track record – results by turbine type. [Online]. Available: https://www.vestas.com/en/products/track_record

[5] Z. Dong, Z. Li, L. Du, Y. Liu, and Z. Ding, "Coordination strategy of large-scale DFIG-based wind farm for voltage support with high converter capacity utilization," *IEEE Trans. Sustain. Energy*, vol. 12, no. 2, pp. 1416–1425, Apr. 2021.

[6] R. H. Yang and J. X. Jin, "Unified power quality conditioner with advanced dual control for performance improvement of DFIG-based wind farm," *IEEE Trans. Sustain. Energy*, vol. 12, no. 1, pp. 116–126, Jan. 2021.

[7] *IEEE Standard for Interconnection and Interoperability of Distributed Energy Resources with Associated Electric Power Systems Interfaces*, IEEE Std 1547™-2018, 2018.

[8] A. Dida, F. Merahi, and S. Mekhilef, "New grid synchronization and power control scheme of doubly-fed induction generator based wind turbine system using fuzzy logic control," *Comput. Electr. Eng.*, vol. 84, pp. 1–18, Jun. 2020.

[9] L. Xiong, P. Li, F. Wu, M. Ma, M. W. Khan, and J. Wang, "A coordinated high-order sliding mode control of DFIG wind turbine for power optimization and grid synchronization," *Int. J. Electr. Power Energy Syst.*, vol. 105, pp. 679–689, Sep. 2019.

[10] Y. Zhang, T. Jiang, and J. Jiao, "Model-free predictive current control of a DFIG using an ultra-local model for grid synchronization and power regulation," *IEEE Trans. Energy Convers.*, vol. 35, no. 4, pp. 2269–2280, Dec. 2020.

[11] G. Yuan, J. Chai, and Y. Li, "Vector control and synchronization of doubly fed induction wind generator system," in *Proc. 4th Int. Conf. IPEMC*, vol. 2, 2004, pp. 886–890.

[12] A. G. Abo-Khalil, D.-C. Lee, and S.-H. Lee, "Grid connection of doubly-fed induction generators in wind energy conversion system," in *Proc. 5th Int. Conf. IPEMC*, vol. 3, 2006, pp. 1–5.

[13] G. Tapia, G. Santamaría, M. Telleria, and A. Susperregui, "Methodology for smooth connection of doubly fed induction generators to the grid," *IEEE Trans. Energy Convers.*, vol. 24, no. 4, pp. 959–971, Dec. 2009.

[14] A. G. Abo-Khalil, "Synchronization of DFIG output voltage to utility grid in wind power system," *Renew. Energy*, vol. 44, pp. 193–198, Aug. 2012.

[15] X. Zhang, D. Xu, Y. Lang, and H. Ma, "Study on stagewise control of connecting DFIG to the grid," in *Proc. 5th Int. Conf. IPEMC*, vol. 1, 2006, pp. 1–5.

[16] J.-W. Park, K.-W. Lee, D.-W. Kim, K.-S. Lee, and J.-S. Park, "Control method of a doubly-fed induction generator with a grid synchronization against parameter variation and encoder position," in *Conf. Rec. Ind. Appl. Soc. IEEE-IAS Annu. Meet.*, 2007, pp. 931–935.

[17] A. M. Eltamaly, M. Al-Saud, K. Sayed, and A. G. Abo-Khalil, "Sensorless active and reactive control for DFIG wind turbines using opposition-based learning technique," *Sustainability*, vol. 12, no. 9, pp. 1–14, Apr. 2020.

[18] S. Arnaltes-Gómez and J. L. Rodríguez-Amenedo, "Grid synchronisation of doubly fed induction generators using direct torque control," in *Proc. 28th Annu. Conf. IECON*, vol. 4, 2002, pp. 3338–3343.

[19] J. Arbi, M. J.-B. Ghorbal, I. Slama-Belkhodja, and L. Charaabi, "Direct virtual torque control for doubly fed induction generator grid connection," *IEEE Trans. Ind. Electron.*, vol. 56, no. 10, pp. 4163–4173, Oct. 2009.

[20] G. Iwanski and W. Koczara, "DFIG-based power generation system with UPS function for variable-speed applications," *IEEE Trans. Ind. Electron.*, vol. 55, no. 8, pp. 3047–3054, Aug. 2008.

[21] A. Thakallapelli, S. Kamalasadan, K. M. Muttaqi, and M. T. Hagh, "A synchronization control technique for soft connection of doubly fed induction generator based wind turbines to the power grids," *IEEE Trans. Ind. Appl.*, vol. 55, no. 5, pp. 5277–5288, Sep. 2019.

[22] J. L. Elizondo, A. Olloqui, M. Rivera, M. E. Macias, O. Probst, O. M. Micheloud, and J. Rodriguez, "Model-based predictive rotor current control for grid synchronization of a DFIG driven by an indirect matrix converter," *IEEE J. Emerg. Sel. Topics Power Electron.*, vol. 2, no. 4, pp. 715–726, Dec. 2014.

[23] S. Z. Chen, N. C. Cheung, K. C. Wong, and J. Wu, "Grid synchronization of doubly-fed induction generator using integral variable structure control," *IEEE Trans. Energy Convers.*, vol. 24, no. 4, pp. 875–883, Dec. 2009.

[24] A. Abdelbaset, A.-H. M. El-Sayed, and A. E. H. Abozeid, "Grid synchronisation enhancement of a wind driven DFIG using adaptive sliding mode control," *IET Renew. Power Gener.*, vol. 11, no. 5, pp. 688–695, Apr. 2017.

[25] A. Susperregui, M. I. Martinez, G. Tapia, and I. Vechiu, "Second-order sliding-mode controller design and tuning for grid synchronisation and power control of a wind turbine-driven doubly fed induction generator," *IET Renew. Power Gener.*, vol. 7, no. 5, pp. 540–551, Nov. 2012.

[26] *IEEE Recommended Practice and Requirements for Harmonic Control in Electric Power Systems*, IEEE Std 519™-2014, 2014.

[27] G. F. Gontijo, T. C. Tricarico, B. W. França, L. F. da Silva, E. L. van Emmerik, and M. Aredes, "Robust model predictive rotor current control of a DFIG connected to a distorted and unbalanced grid driven by a direct matrix converter," *IEEE Trans. Sustain. Energy*, vol. 10, no. 3, pp. 1380–1392, Jul. 2019.

[28] I. Villanueva, A. Rosales, P. Ponce, and A. Molina, "Grid-voltage-oriented sliding mode control for DFIG under balanced and unbalanced grid faults," *IEEE Trans. Sustain. Energy*, vol. 9, no. 3, pp. 1090–1098, Jul. 2018.

[29] L. Shang and J. Hu, "Sliding-mode-based direct power control of grid-connected wind-turbine-driven doubly fed induction generators under unbalanced grid voltage conditions," *IEEE Trans. Energy Convers.*, vol. 27, no. 2, pp. 362–373, Jun. 2012.

[30] C. Liu, F. Blaabjerg, W. Chen, and D. Xu, "Stator current harmonic control with resonant controller for doubly fed induction generator," *IEEE Trans. Power Electron.*, vol. 27, no. 7, pp. 3207–3220, Jul. 2012.

[31] S. Z. Chen, N. C. Cheung, Y. Zhang, M. Zhang, and X. M. Tang, "Improved grid synchronization control of doubly fed induction generator under unbalanced grid voltage," *IEEE Trans. Energy Convers.*, vol. 26, no. 3, pp. 799–810, Sep. 2011.

[32] A. M. Eltamaly, M. S. Al-Saud, and A. G. Abo-Khalil, "Dynamic control of a DFIG wind power generation system to mitigate unbalanced grid voltage," *IEEE Access*, vol. 8, pp. 39 091–39 103, Feb. 2020.

[33] A. Khan, X. M. Hu, M. A. Khan, and P. Barendse, "Doubly fed induction generator open stator synchronized control during unbalanced grid voltage condition," *Energies*, vol. 13, no. 12 (3155), pp. 1–13, Jun. 2020.

[34] N.-B. Lai and K.-H. Kim, "Robust control scheme for three-phase grid-connected inverters with LCL-filter under unbalanced and distorted grid conditions," *IEEE Trans. Energy Convers.*, vol. 33, no. 2, pp. 506–515, Jun. 2018.

[35] P. Vas, *Sensorless Vector and Direct Torque Control*. New York, USA: Oxford University Press, 1998.

[36] M. I. Martinez, A. Susperregui, and G. Tapia, "Second-order sliding-mode-based global control scheme for wind turbine-driven DFIGs subject to unbalanced and distorted grid voltage," *IET Electr. Power Appl.*, vol. 11, no. 6, pp. 1013–1022, Jul. 2017.

[37] A. Levant, "Sliding order and sliding accuracy in sliding mode control," *Int. J. Control*, vol. 58, no. 6, pp. 1247–1263, Aug. 1993.

[38] V. Utkin, J. Guldner, and J. Shi, *Sliding Mode Control in Electromechanical Systems*. London, UK: Taylor & Francis, 1999.

[39] L. Xu, "Coordinated control of DFIG's rotor and grid side converters during network unbalance," *IEEE Trans. Power Electron.*, vol. 23, no. 3, pp. 1041–1049, May 2008.

[40] R. Peña, R. Cárdenas, J. Proboste, G. Asher, and J. Clare, "Sensorless control of doubly-fed induction generators using a rotor-current-based MRAS observer," *IEEE Trans. Ind. Electron.*, vol. 55, no. 1, pp. 330–339, Jan. 2008.

[41] O. S. Senturk and A. M. Hava, "A simple sag generator using SSRs," *IEEE Trans. Ind. Appl.*, vol. 48, no. 1, pp. 172–180, Jan. 2012.